Effect of Mn on microstructure and corrosion properties of extruded Mg-1%Zn alloy

Z M Zhang[1,2], Y Ma[1], Z Z Xi[2], C J Xu[1] and Z L Lv[1]

[1] School of Materials Science and Engineering, Key Laboratory of Electrical Materials and Infiltration Technology of Shaanxi Province, Xi'an University of Technology, Xi'an 710048，China
[2] School of Materials and Chemical Engineering, Shaanxi Key Laboratory of Optoelectronic Functional Materials and Devices, Xi'an Technological University, Xi'an, 710032, China

Email: rainmy905@163.com

Abstract. The microstructure of the extruded Mg-1Zn alloy doped with different content of manganese was analyzed by optical microscopy, scanning electron microscopy with energy dispersive X-ray spectroscopy and X-ray diffractometry. The mass-loss immersion method and electrochemical test were used to evaluate the corrosion properties. The results show that the microstructure of the extruded Mg-1%Zn-*x*%Mn (mass fraction, *x*=0.4, 0.8, 1.2） alloys consists of α-Mg and α-Mn, the grain size of α-Mg decreases with increasing Mn content. Electrochemical corrosion behavior of the alloys is similar. Mn has considerable effect on the corrosion rate, the corrosion process is exacerbated by the galvanic corrosion occurred at interface between α-Mg and α-Mn. The corrosion rate increases as the Mn content increases. Mg-1%Zn-0.4% Mn alloy exhibits the best corrosion resistance between the Mg-1%Zn-*x*%Mn alloys

1. Introduction

Magnesium alloys show potential application as degradable hard tissue implant materials due to their good biocompatibility and mechanical properties. Meanwhile, Mg alloys have the advantage that they do not show the undesirable effect of stress shielding, which occurs normally in conventional metallic implants made of stainless steel or titanium alloy which are widely used for bone implants [1,2]. It is expected that Mg alloys can be applied as lightweight, degradable load bearing orthopedic implant materials [3]. Thus, more researches have been focused on the study of biomedical Mg alloys [3,4]. However, the mechanical property of pure Mg is too low. Furthermore, pure magnesium corrodes too quickly in physiological system, and may lose mechanical integrity before tissues have sufficiently healed. Alloying is an important way to promote mechanical properties and corrosion resistance of Mg alloys [5]. The common alloying elements include Al, Zn, Mn, Ca and rare-earth. While toxicity researches about Zn, Mn have shown no harm to the human health [6].

The equilibrium solid solubility of Zn in Mg at eutectic temperature is around 6.2%, and it decreases with temperature [7]. In smaller amounts, Zn contributes to strength due to solid solution strengthening, it also acts, to some extent, as a grain refining agent and additionally contributes to grain boundary strengthening [6]. A study conducted by Song et al showed that the addition of Zn in pure Mg can significantly reduce corrosion rate [5]. But larger amounts (>2.0%) of Zn leads to a

decrease of the corrosion resistance [6]. Zn is a essential element for bone metabolism [8]. As an active center for hundreds of enzymes, Zn element can promote cell renewing and healing of surgical wound [9]. However, it is believed that the released Mg ions may show a toxic effect on cells at high concentration. As a result, Zn content in biodegradable Mg alloys should not excess 2.0% [10].

Mn is mainly used to enhance ductility and strength [6,11], and can also improve heat resistance of Mg alloys and refine the grain size [7]. More important, Mn addition transforms Fe and other impurities into relatively harmless intermetallic compounds and can therefore be used to control the corrosion of magnesium alloys [6-7]. Mn can replace Zr additives in Mg-Zn-based alloys to reduce cost[7]. Mn is also one of the essential trace elements in bodies.

Mg-Zn alloys and Mg-Mn alloys have been investigated as biodegradable materials and have shown good biocompatibility [2,12]. Mg-Zn based alloys possess high yield strength and load capacity, and are especially suitable for high strength applications. Mn addition can improve casting property and plastic forming ability of Mg-Zn alloys [13]. Considerable attention has been focused on Mg-Zn-Mn wrought magnesium alloys, since high strength can be achieved after thermal processing [14]. Furthermore, Mg-Zn-Mn wrought alloys have advantage of low density, relatively high specific strength and stiffness, and can meet the requirement of light-weight construction. On the other hand, Mg-Zn-Mn alloys contain no rare earth elements and noble metal elements such as Zr, so lower cost can simply make them more widespread [14].

Mg-Zn-Mn alloys exhibite good biocompatibility [2]. Xu et al.[1] fabricated a Mg-Mn-Zn alloy with good mechanical and corrosion resistance properties. The study on corrosion behavior of hot extruded Mg-1Mn-1Zn alloy in 0.9% sodium chloride water solution showed that extrusion deformation can improve corrosion resistance [15]. Zhou et al. investigated the microstructure, mechanical property, corrosion behavior and biocompatibility of extruded Mg-Mn-Zn-Nd alloys [16]. The extruded alloys show good biocompatibility and much higher corrosion resistance than that of cast pure Mg. The extruded Mg-1Mn-2Zn-1.0Nd alloy shows a great potential for biomedical applications due to the combination of enhanced mechanical properties, high corrosion resistance and good biocompatibility [16]. The addition of cerium in Mg-2Zn-0.5Mn-1Ca alloy can enhance its in-vitro biocorrosion resistance and reduce its degradation rate. The alloy containing 1.35 % Ce has the potential to be used as future biomaterials [6]. Wang et al. fabricated a novel interpenetrating β-TCP/Mg-Zn-Mn composite by infiltrating Mg-Zn-Mn alloy into porous β-TCP [2]. The ultimate compressive strength of the composite is near with the natural bone. The electrochemical and immersion tests indicated that the corrosion resistance of the composite is better than that of the Mg-Zn-Mn matrix alloy [2].

Up to now, most researches have being concentrated on the effect of Mn on mechanical properties of Mg-Zn based alloys. A few of studies reported the role of Mn in Mg alloys, whereas the investigation of its effect on corrosion resistance is less, especially in physiological environment. On the basis of the previous studies, the corrosion behavior of extruded Mg-1%Zn-*x*%Mn alloys (mass fraction, *x*=0.4, 0.8, 1.2） in SBF solution (one of the simulated body fluids) was investigated by mass-loss immersion method and electrochemical test in the present paper, so as to provide reference for the application of the Mg alloys as degradable hard tissue implant materials.

2. Experimental

2.1. Alloy preparation

Commercial high-purity Mg ingot (>99.98%), zinc chip (>99.99%) and Mg-10%Mn master alloy were used to prepare the Mg-1%Zn-*x*%Mn alloys. All alloys were melted in a pit type electronic resistance furnace in a titanium crucible. When the melts were prepared, they were cast into a water-cooled copper mold with an ingot diameter of 51 mm. The melting, pouring, freezing and cooling process were all conducted under argon atmosphere. The ingots were then processed by a homogenization treatment, i.e. homogenized at 330 ℃ for 10 h and then furnace cooled. After that, the ingots were

machined into rods of 49.5 mm diameter and 95 mm length, and then hot extruded into round bars of diameter of 16.5 mm at 320 ℃ with a ram speed of 20 mm/min and extrusion ratio of 9:1.

2.2. Corrosion property testing

Corrosion property of the experimental alloys was investigated by static immersion method and electrochemical test using SBF solution as corrosion medium.

The dimension of the immersion samples is 3 mm in height and 15 mm in diameter. The samples were abraded with SiC paper down to grade 1200, ultrasonically rinsed with acetone and washed completely with distilled water, and then dried at room temperature. Then the weights were measured by a electric balance with precision of 0.1 mg. All samples were immersed in SBF solution at 37 ℃ for 72 h. Then the samples were weighed again after the corrosion products were removed completely. Corrosion rate R was calculated according to equation (1):

$$R = \frac{8.76\times10^{7}\times\left(m_0 - m_1\right)}{St\rho} \qquad (1)$$

where R is corrosion rate, mm/a; m_0 and m_1 are weights of the samples before and after immersion, respectively, g; S is surface area of the samples exposed to the corrosive media, cm^2; t is the exposure time, t=72 h; ρ is the density of the samples, ρ=1.74 g/cm^3.

Cylindrical samples (12 mm diameter and 10 mm height) were used to perform the potentiodynamic polarization test. The end surfaces of the samples were vertical to extrusion direction. Except for one end surface, the samples were molded into mixed resin (epoxy resin/polyamide resin=1:1). A three-electrode cell was used for potentiodynamic polarization test by Electrochemical Workstation CS-310. The working electrode was the sample, the counter electrode was made of platinum and the reference electrode was saturated calomel electrode (SCE). The test was conducted at 37 ℃ in open air in a three necked round bottom flask containing 250 ml SBF solution. Prior to potentiodynamic polarization test, the samples were soaked in the solution for 10 min. All experiments were carried out at a constant scan rate of 0.5 mV/s from -100 mV SCE to 100 mV SCE.

2.3. Microstructure and corrosion morphology observation

Cross-sectional microstructures of the extruded bars were examined by optical microscopy (Olympus GX71) after etching with 4% nital solution. The distribution and surface morphology of secondary phase were observed by the scanning electron microscope JSM-6390A with an energy dispersion microanalysis system (EDS). A Shimadzu XRD-7000 X-ray diffractometer (XRD) was used to identify chemical constitution.

The observation of corrosion product morphology was carried out by SEM after the samples were removed from the SBF solution, gently rinsed with distilled water and air dried completely. For the characterization of the surface appearance of corroded specimens, it was conducted after the corrosion products were completely removed.

3. Results and discussion

3.1. Microstructure and phase constitution

Figure 1 shows the OM microstructure of the hot extruded Mg-1%Zn-*x*%Mn alloys with different Mn content. It can be seen obviously that the microstructure consists of nearly equiaxed grains, and the grain size decreases with increasing Mn content. In addition, the streamlines resulted from the extrusion deformation are also discernible (figure 1a). This phenomenon indicates that the incomplete dynamic recrystallization occurred during extrusion and thus resulted in equiaxed grains.

Figure 2 shows that the predominant phase of the Mg-1%Zn-*x*%Mn alloys is α-Mg phase. According to the binary Mg-Zn diagram[17], it can be observed that up to 2.0%Zn can completely dissolve in α-Mg. Thus, no any compound was found in Mg-Zn alloy. Meanwhile, no Mn peaks

appeared in figure 2, this is because the amount of Mn is too little to be detected. Comparing the 2θ angles of α-Mg with that of pure Mg[1], one will see that the 2θ angles of α-Mg are smaller than that of pure Mg. Evidently, the difference of 2θ angles arises from the lattice deformation of Mg that was resulted from the solid solution of Zn which enlarged the crystal plane spacing.

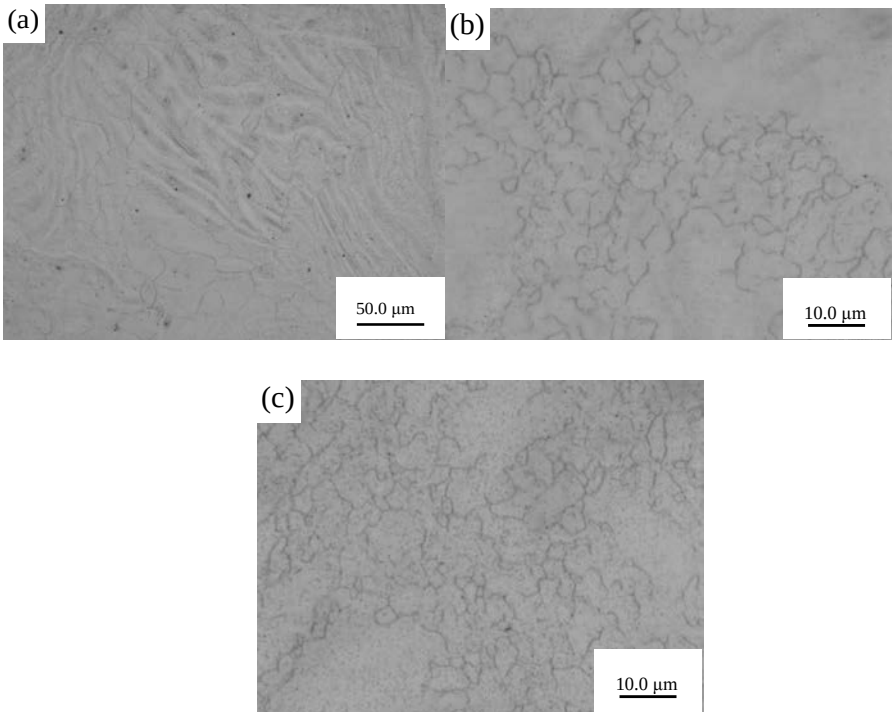

Figure 1. OM microstructures of the hot extruded Mg-1%Zn-*x*%Mn alloys with different content of Mn. (a) *x*=0.4Mn, (b) *x*=0.8Mn, (c) *x*=1.2Mn.

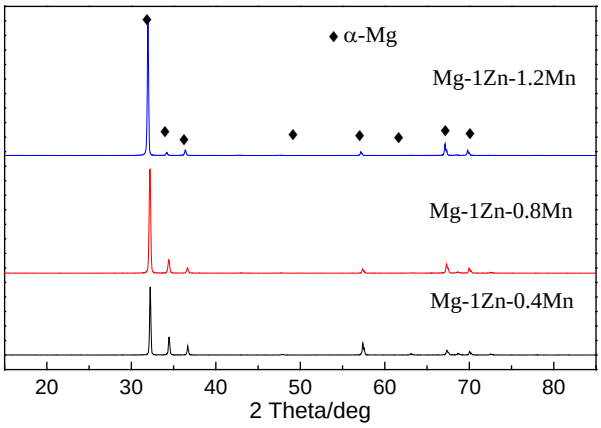

Figure 2. XRD pattern of Mg-1%Zn-*x*%Mn alloys with different content of Mn.

Figure 3 shows the SEM microstructures of the alloys under high magnification and EDS results. Bright secondary phases with small size are clearly visible. EDS results shown that except for Mg, higher content of Mn exists in the secondary phase. Detecting trace compositions in small sized particles by microstructural observation is often associated with high difficulties[17]. Considering small size of the bright secondary phases (less than 0.5 μm), the microzone of EDS analysis may cover part

of α-Mg, this is the reason why high content of Mg was detected in the secondary phases. According to Mg-Mn binary phase diagram, very limited solubility of Mn in Mg and negligible solubility of Mg in Mn are observed, and no intermetallic compound is reported in Mg-Mn system[17], therefore it is certain that the secondary phase in the alloys is α-Mn.

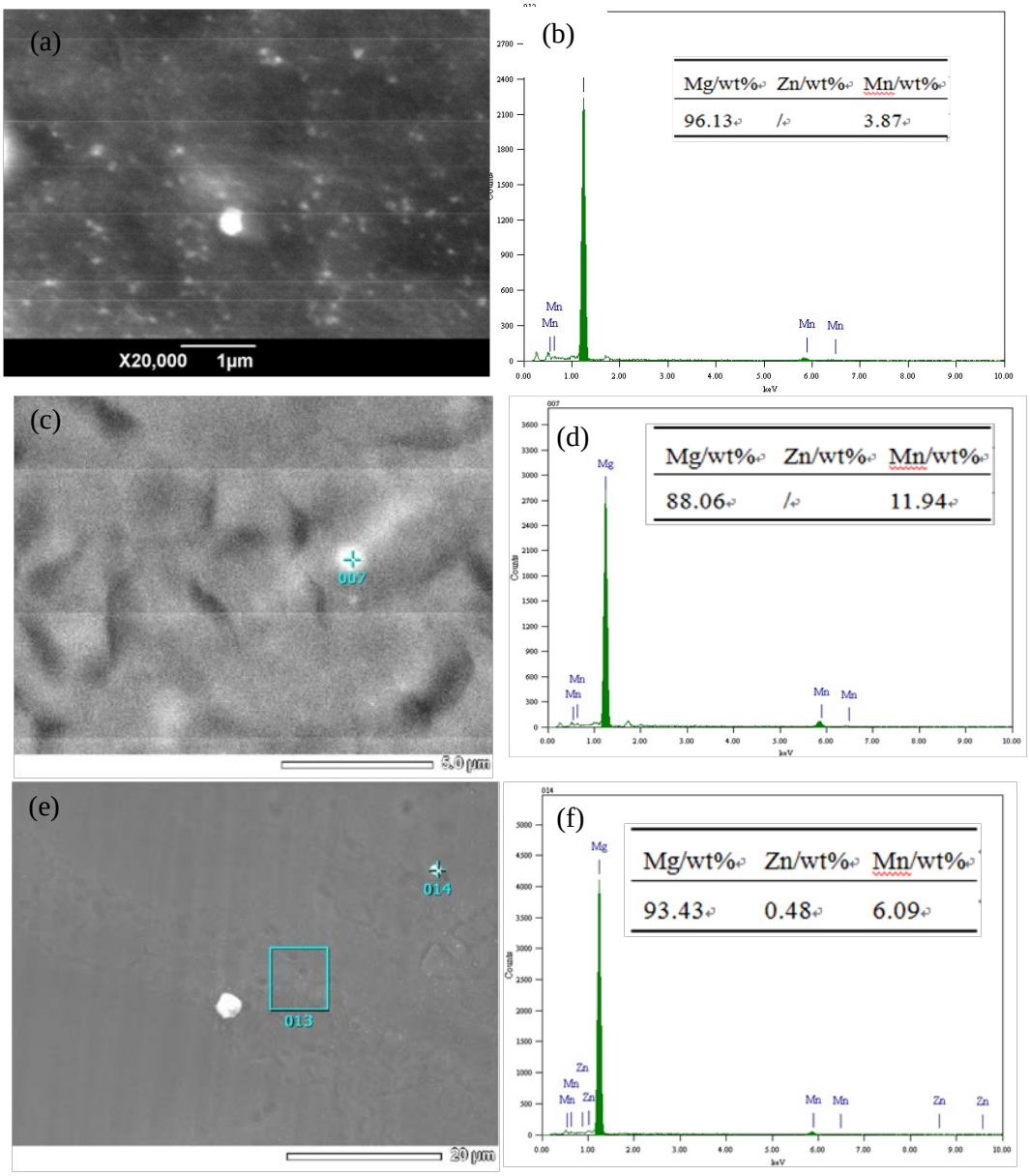

Figure 3. Secondary phases (shown by arrows) and their EDS results in the Mg-1%Zn-*x*%Mn alloys with different Mn content. (a,b) *x*=0.4Mn; (c,d) *x*=0.8Mn; (e,f) *x*=1.2Mn.

According to Mg-Zn binary phase diagram [17], the maximum solubility of Zn in Mg is about 6.2%. As temperature decreases, the solubility decreases prominently and changes to around 2.0% at ambient temperature. Consequently, the microstructure of Mg-1Zn alloy is composed of α-Mg. No any other secondary phase form by further processing. It can be known from Mg-Mn binary phase diagram [17] that the maximum solubility of Mn in Mg is about 2.2%, and decreases to below 0.1% at room temperature. As a result, α-Mn may precipitate from α-Mg during cooling process.

Very few experimental works on the Mg-Mn-Zn alloys are available in the literature, no ternary compound could be found in the literature [17]. According to Mg-Mn-Zn ternary phase diagram [17],

the primary phase of the Mg-1%Zn-*x*%Mn alloys is α-Mg. The solubilities of Zn and Mn in Mg all decrease with temperature decreasing. For example, the solubility of Zn and Mn in Mg is 6.2% and 0.52% at 347 ℃, and decrease to 3.9% and 0.07% respectively at 250 ℃. Therefore, the equilibrium microstructure of the Mg-1%Zn-*x*%Mn alloys at ambient temperature consists of α-Mg and α-Mn. In the present study, Mg-1%Zn-*x*%Mn alloys solidified and cooled in a water-cooled copper mold, the corresponding freezing rate and cooling velocity were relatively high, and Mn and Zn were all dissolved in α-Mg after solidification. Therefore, α-Mn phases in the alloys (figure 3) would be precipitated during cooling period. Another possibility is that α-Mn phase may also precipitate during homogenization treatment, hot extrusion and following cooling process. Whereas, because of small amount of α-Mn and its small size, no diffraction peak of α-Mn was detected in XRD analysis.

It is proved that the dispersed tiny α-Mn particles can impede dynamic recrystallization and hinder growth of recrystallized grains [8,11]. As a result, the grain size of Mg-1%Zn-*x*%Mn alloys decreased as Mn content increasing.

3.2. Immersion corrosion behavior

Figure 4 reveals the average corrosion rate of the extruded Mg-1%Zn-*x*%Mn alloys measured by mass-loss method after immersion in SBF solution at 37 ℃ for 72 h. It can be seen that the corrosion rate of Mg-1Zn-0.4Mn alloy is the lowest (4.23 mm/a). As Mn content increases, the corrosion rate increases and thus the corrosion resistance declines. The highest corrosion rate is observed for Mg-1Zn-1.2Mn alloy (4.92 mm/a).

Figure 5 shows the potentiodynamic polarization curves of the alloys in SBF solution. In general, cathodic polarization curve is assumed to indicate hydrogen evolution via water reduction, however the anodic polarization curve exhibites the dissolution of Mg [18]. It appears that the shape of the polarization curves is similar, this indicates that the dynamic behavior of electrochemical corrosion reaction in the alloys is similar too. It can be found from the shape of anodic polarization curves that no passive region appears. This means that the Mg alloys were electrochemically active during the early stage of corrosion in SBF solution. No protective film formed on the surface of the sample.

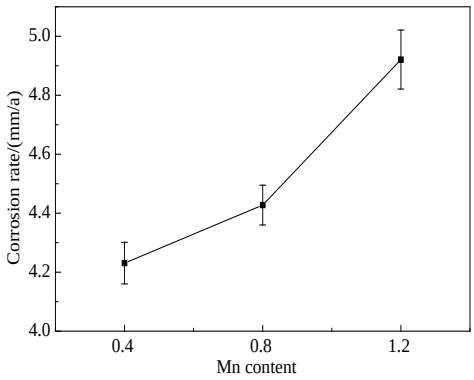

Figure 4. Average corrosion rate of the extruded Mg-1%Zn-*x*%Mn alloys with different Mn content immersed in SBF solution for 72h.

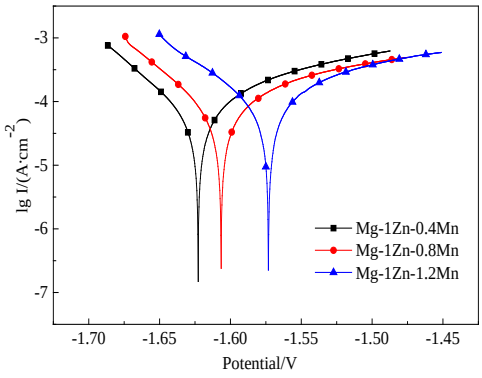

Figure 5. The potentiodynamic polarization curves of the extruded Mg-1%Zn-*x*%Mn alloys with different Mn content.

Table 1 lists the electrochemical parameters calculated from the polarization curves (figure 5) by traditional Tafel fitting. It shows that the self corrosion potential of the alloys shift towards nobler direction with increasing Mn content. Mg-1Zn-0.4Mn alloy exhibits the lowest corrosion potential of about -1.619 V. By addition of 1.2% Mn, the corrosion potential shifts towards nobler direction (-1.578 V SCE), which is about 41 mV nobler than that of Mg-1Zn-0.4Mn alloy. The corrosion current

density of Mg-1Zn-0.4Mn alloy is 0.111 mA/cm^2, which is nearly the same with that of Mg-1Zn-0.8Mn alloy (0.122 mA/cm^2). It should be noted that all of them are much lower than that of Mg-1Zn-1.2Mn alloy (0.213 mA/cm^2). This indicates that Mn has considerable effect on the corrosion rate of the alloys. The corrosion rate of Mg-1Zn-1.2Mn is 4.72 mm/a which is nearly twice than that of Mg-1Zn-0.4Mn alloy (2.44 mm/a). The electrochemical test illustrates that the corrosion resistance of Mg-1Zn-0.4Mn alloy is the highest, this result is consistent with the mass-loss immersion test. It was reported [19] that the corrosion current density and corrosion rate of rolled Mg-1Zn alloy are 0.041 mA/cm^2 and 0.92 mm/a, respectively. By comparison with Mg-1Zn-0.4Mn alloy, Mg-1Zn has less current density and lower corrosion rate. This phenomenon confirms the significant effect of Mn on the corrosion behavior of the alloys. As Mn content increases, the corrosion rate increases.

Table 1. Electrochemical parameters of Mg-1%Zn-x%Mn alloys in SBF solution.

Alloy	Corrosion potential (V)	Corrosion current density I (mA.cm^{-2})	Corrosion rate (mm.a^{-1})
Mg-1Zn-0.4Mn	-1.619	0.111	2.455
Mg-1Zn-0.8Mn	-1.602	0.122	2.699
Mg-1Zn-1.2Mn	-1.578	0.213	4.720

3.3. Corrosion morphology observation

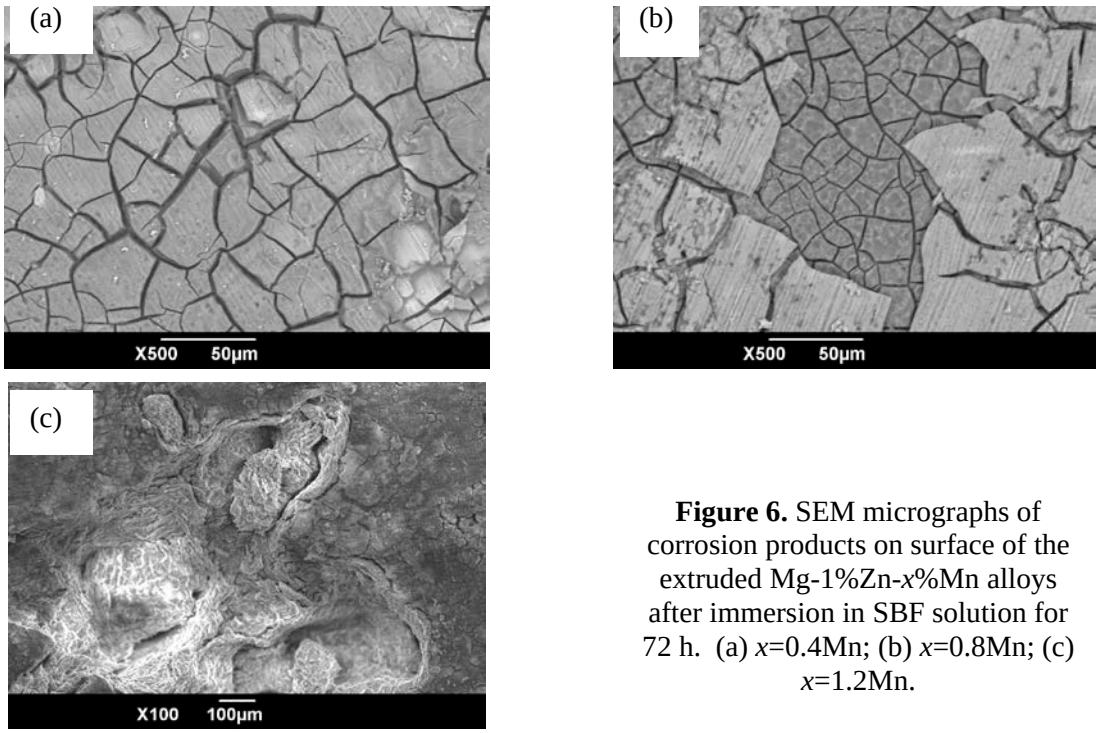

Figure 6. SEM micrographs of corrosion products on surface of the extruded Mg-1%Zn-*x*%Mn alloys after immersion in SBF solution for 72 h. (a) *x*=0.4Mn; (b) *x*=0.8Mn; (c) *x*=1.2Mn.

Figure 6 shows the morphologies of corrosion product of the Mg-1%Zn-*x*%Mn alloys. During the early stage, the alloys were electrochemically active, no protective layer formed. However, as corrosion proceeded, more and more corrosion product produced and accumulated which led to the formation of a protective layer on the surface of the samples. It can be seen from figure 6 that the surface of Mg-1Zn-1.2Mn was covered with a layer of corrosion product accompanied by deep and large pits, which indicates that serious corrosion occurred. Whereas, no obvious corrosion pits were found on the corrosion product layer of Mg-1Zn-0.4Mn alloy, and slight peeling of corrosion products were observed for Mg-1Zn-0.8Mn alloy. The network-like cracks can probably be attributed to the dehydration of corrosion product layer after removal of the samples from the test solution and drying in warm air [1].

The surface morphologies of the soaked samples after removal corrosion product are depicted in figure 7. Obviously, corrosion pits and filiform corrosion took place on the alloys. The filiform corrosion on Mg-1Zn-0.4Mn alloy is clearly visible and distributes along the deform streamlines. This phenomenon demonstrates that corrosion proceeded in a certain direction. For Mg-1Zn-0.8Mn alloy, there are a few of shallow corrosion pits and superficial filiform corrosion. However, besides the filiform corrosion, a few deep corrosion pits appear on Mg-1Zn-1.2Mn sample surface. Therefore, it can be concluded that the corrosion severity is in order of Mg-1Zn-0.4Mn, Mg-1Zn-0.8Mn and Mg-1Zn-1.2Mn after 72 h of immersion in SBF solution. Mg-1Zn-1.2Mn alloy corroded heavily as indicated by deep corrosion pits, this led to the highest corrosion rate.

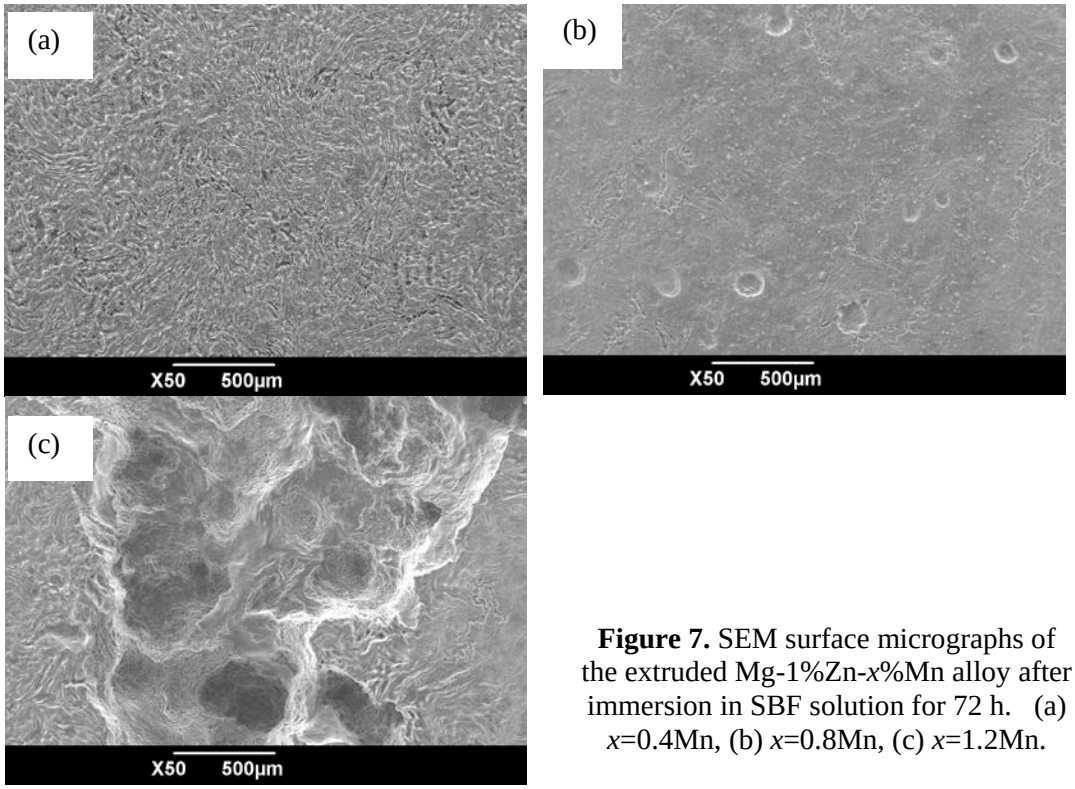

Figure 7. SEM surface micrographs of the extruded Mg-1%Zn-*x*%Mn alloy after immersion in SBF solution for 72 h. (a) *x*=0.4Mn, (b) *x*=0.8Mn, (c) *x*=1.2Mn.

The standard corrosion potentials of Mg, Mn, Zn are -2.37 V, -1.182 V and -0.762 V. The corrosion potential of α-Mg containing small amount of Zn or Mn is slightly higher than that of pure Mg [15,20], thus the addition of Mn reduced the corrosion rate of the Mg alloys. Microgalvanic corrosion plays a dominate role in corrosion. The corrosion potential of α-Mn is much higher than that of α-Mg. Therefore, α-Mn acted as cathode in microgalvanic corrosion. Precipitation of α-Mn promoted cathode process and resulted in the movement of corrosion potential of α-Mn to a nobler direction. As a result, microgalvanic corrosion was exacerbated.

From the result of the electrochemical experiment (figure 5), one can see that no protective layer formed at early corrosion stage. Whereas, as the corrosion proceeded, more and more corrosion products accumulated, and eventually the sample was completely coated. As a result, the corrosion product layer could protect the sample from being corroded to some extent, and decreased the corrosion rate to some extent. The quantity and area of minor corrosion pits under corrosion product layer increased with immersion period, which led to the formation of filiform corrosion. The corrosion product layer was porous and loose, and could not prohibit the corrosion reaction effectively. Consequently, corrosion continued, and thus large and deep corrosion pits were formed.

It was reported in reference [15] that the corrosion rate of Mg alloy decreases with immersion time, i.e., corrosion rate is time-dependent. This result explains why the corrosion rates from electrochemical test and immersion test are different, the reason is that corrosion rate in

electrochemical test is a instantaneous value, while corrosion rate in immersion test is an average value for 72h.

4. Conclusions

(1) The Zn and Mn elements in Mg-1%Zn-*x*%Mn alloys (mass fraction, *x*=0.4, 0.8, 1.2） can dissolve completely in α-Mg during solidification, whereas Mn precipitates as α-Mn during cooling period. The microstructure of Mg-1%Zn-*x*%Mn alloys is composed of α-Mg and α-Mn. The grain size decreases with increasing Mn content.

(2) Mn has considerable effect on the corrosion rate of the alloys. The corrosion process is exacerbated by the galvanic corrosion occurred at interfaces between α-Mg and α-Mn. As Mn content increases, the corrosion rate increases. Mg-1Zn-0.4Mn exhibits best corrosion resistance.

(3) Electrochemical corrosion behavior of the Mg-1%Zn-*x*%Mn alloys is similar, no passivation occurs during corrosion process. The alloys are highly electrochemically active, and the effectively protective layer cannot form during corrosion.

Acknowledgments

This work was financially supported by the Shaanxi provincial project of special foundation of key disciplines, the research project of Shaanxi Key Laboratory of Optoelectronic Functional Materials and Devices (No.ZSKJ201403) and the scientific research project of Education Department of Shaanxi Province (No.2013JK0906)

References

[1] Wang X, Dong L H, Ma X L and Zheng Y F 2013 *Mater. Sci. Eng.* C **33**(2) 618–25
[2] Wang X, Zhang P, Dong L H, Ma X L, Li J T and Zheng Y F 2014 *Mater. Design* **54** 995–1001
[3] Mark P S, Alexis M P, Jerawal H and George D 2006 *Biomaterials* **27**(9) 1728–34
[4] Kannan M B and Raman R K 2008 *Biomaterials* **29**(15) 2306–14
[5] Song G L 2006 *Corrosion and protection of magnesium alloys* (Beijing: Chemical industry press) p238
[6] Zhang F, Ma A B, Song D, Jiang J H, Lu F M, Zhang L Y, Yang D H and Chen J Q 2015 *J. Rare Earths* **33**(1) 93–101
[7] Yuan J W, Zhang K, Zhang X H, Li X G, Li T, Li Y J, Ma M L and Shi G L 2013 *J. Alloys & Comp.* **578**(6) 32–36
[8] Zhuang Y, Yu Y D and Pei T 2013 *J. Harbin Univ. Sci. Tech.* **18**(1) 55–60
[9] Zhang S X, Li J N, Song Y, Zhao C L, Zhang X N, Xie C Y, Zhang Y, Tao H R, He Y H, Jiang Y and Bian Y J 2009 *Mater. Sci. Eng.* C **29**(6) 1907–19
[10] Yu G, Liu Y L, Li Y, Ye L Y, Guo X H and Zhao L 2002 *The Chinese J. Nonferrous Met.* **12**(6) 1087–1098
[11] Zhang D F, Qi F G, Shi G L and Dai Q W 2010 *Rare Met. Mater. Eng.* **39**(12) 2205–10
[12] Zhang S X, Zhang X N, Zhao C L, Li J N, Song Y, Xie C Y, Tao H R, Zhang Y, He Y H, Jiang Y and Bian Y J 2010 *Acta Biomaterialia* **6**(2) 626–40
[13] Zhang D F, Shi G L, Zhao X B and Qi F G 2011 *Mater. Review* **25**(9) 1–10
[14] Zhang D F, Shi G L, Zhao X B and Qi F G 2011 *Trans. Nonferrous Met. Soc. China* **21**(1) 15–25
[15] Zhang Z M, Zhang J, Ma Y, Wang T and Xu C J 2012 *Foundry Technology* **33**(3) 257–60
[16] Zhou Y L, Li Y C, Luo D M, Ding Y F and Hodgson P 2015 *Mater. Sci. Eng.* C **49**(1) 93–100
[17] Ghosh P and Medrag M 2013 *CALPHAD: Computer Coupling of Phase Diagrams and Thermochemistr* **41**(6) 89–107
[18] Chang J W, Guo X W, Fu P H, Peng L M and Ding W J 2007 *Electrochim Acta* **52**(9) 3160–67
[19] Gu X N, Zheng Y F, Cheng Y, Zhong S P and Xi T F 2009 *Biomaterials* **30**(4) 484–498
[20] Chen X Y, Wang J C, Yang G C and Guo Y N 2008 *Foundry Technology* **29**(5) 593–596